Electronic Supplementary Information: Metal Surface Effects on Single Upconverting Nanoparticle Luminescence and Thermometry Signals

Ziyang Ye[a], Laura Signor[b], Molly Cohan[b,c], and Andrea D. Pickel[a,b,d,*]

[a] Materials Science Program, University of Rochester, Rochester, NY 14627

[b] The Institute of Optics, University of Rochester, Rochester, NY 14627

[c] Department of Physics, The College of Wooster, Wooster, OH 44691

[d] Department of Mechanical Engineering, University of Rochester, Rochester, NY 14627

*Corresponding author. Email: apickel@ur.rochester.edu

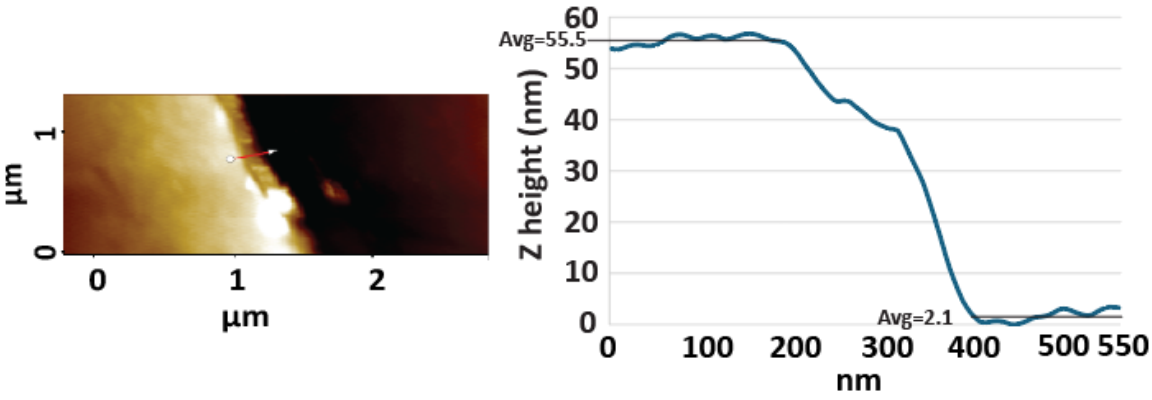

Fig. S1. An atomic force microscope (AFM) was used to obtain a representative thickness measurement for the metal coatings we deposited. A scratch was made in the Au coating, which removed the Au down to the glass substrate over a small region. The AFM was used to measure the z height across the scratch, allowing us to evaluate the coating thickness. This analysis confirmed the film thickness to be approximately 50 nm. The average height on the Au side of the scratch was determined to be approximately 55.5 nm. Meanwhile, the average height on the glass side was determined to be approximately 2.1 nm.

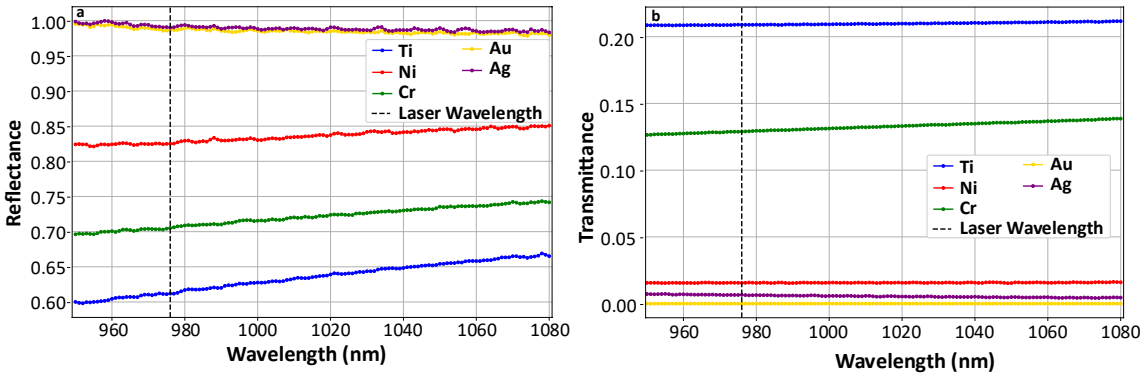

Fig. S2. A PerkinElmer Lambda 900 UV/VIS/NIR spectrometer was used to measure (a) the total reflectance and (b) the transmittance of the metal-coated borosilicate glass substrates for a wavelength range of 800 nm – 1070 nm in 1 nm increments. Measurements were completed on samples coated in the same electron beam evaporation run as the samples used for experiments in the main text, without any UCNPs deposited on them. Since the samples were half coated with metal, a pinhole was used to measure reflectance to ensure the entire laser beam was incident solely on the metal-coated portion of the substrate. The Ag-coated glass substrate had a small scratch in the metal coating, which may have resulted in a higher measured transmittance than is true for the metal coating. The black dashed line represents the laser wavelength of 976 nm that was used for all experiments in the main text.

Metal Coating	Reflectance	Transmittance	Absorptance
Ti	0.6240	0.2089	0.1671
Cr	0.7052	0.1289	0.1659
Ni	0.8250	0.0155	0.1595
Au	0.9866	0.0000	0.0134
Ag	0.9900	0.0066	0.0034

Table S1. Measured reflectance (R), transmittance (T), and calculated absorptance (A) values at 976 nm for each metal coated on a borosilicate glass substrate, shown in order of increasing R. The R and T values were obtained from the data shown in Fig. S2, and A was calculated by $A = 1 - R - T$.

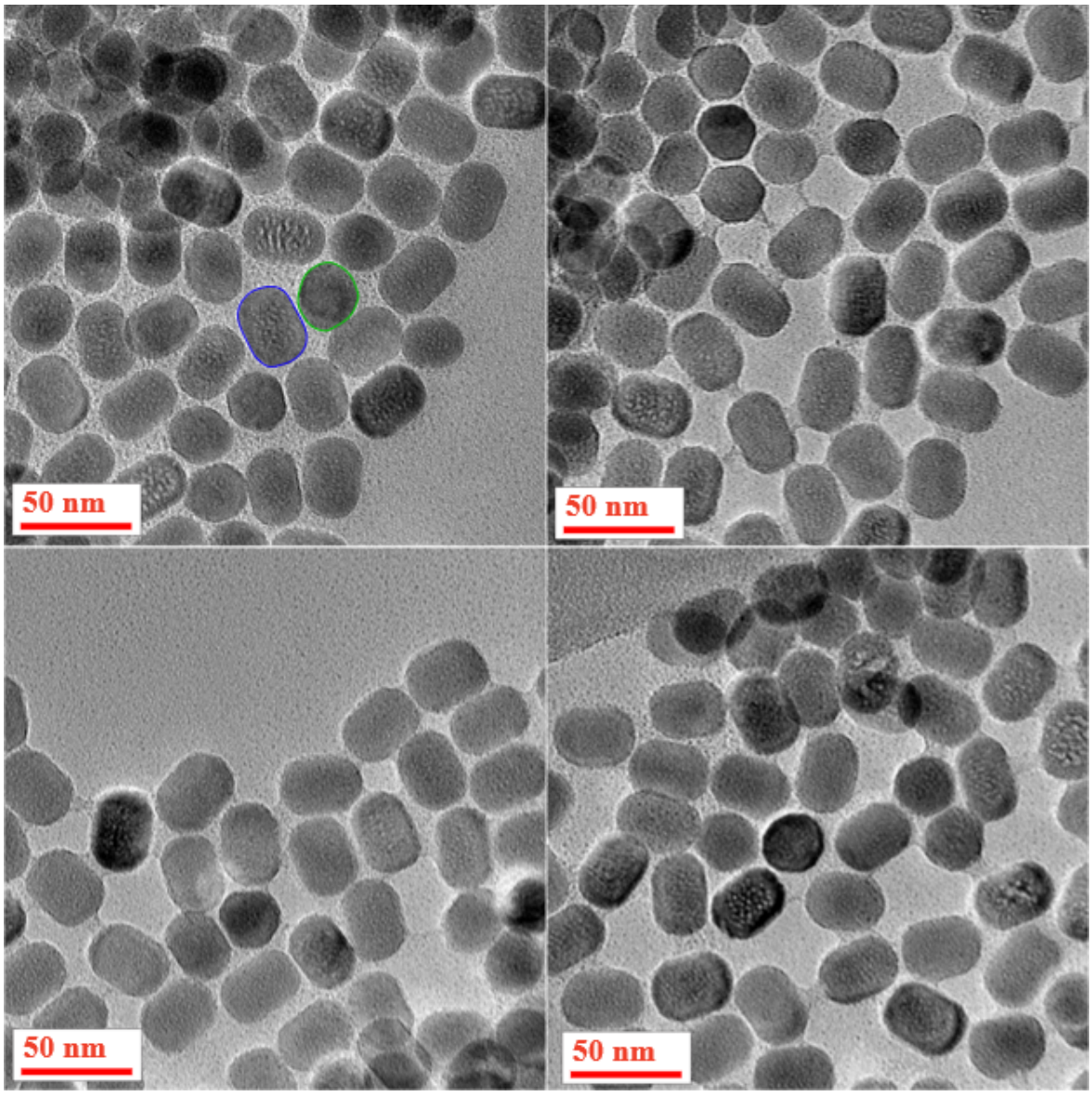

Fig. S3. Four representative transmission electron microscope (TEM) images of the UCNPs used in this work. The UCNPs display varied orientations, landing both on their facets (representative UCNP highlighted in green) and on their sides (representative UCNP highlighted in blue).

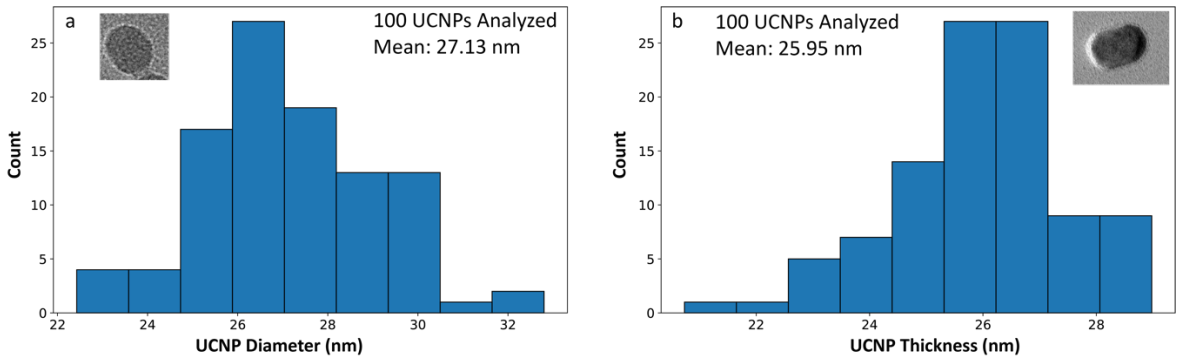

Fig. S4. Transmission electron microscope (TEM) images were analyzed to measure the diameter and thickness of hexagonally faceted UCNPs dispersed on a lacey carbon support grid. When deposited on a TEM grid, the UCNPs naturally exhibit varied orientations, allowing for measurements across their facets (diameter) and along their height (thickness). The histograms in (a) and (b) show distributions of the diameter and thickness, respectively, based on measurements from 100 UCNPs. Insets in (a) and (b) provide representative TEM images illustrating the UCNP orientation in each case.

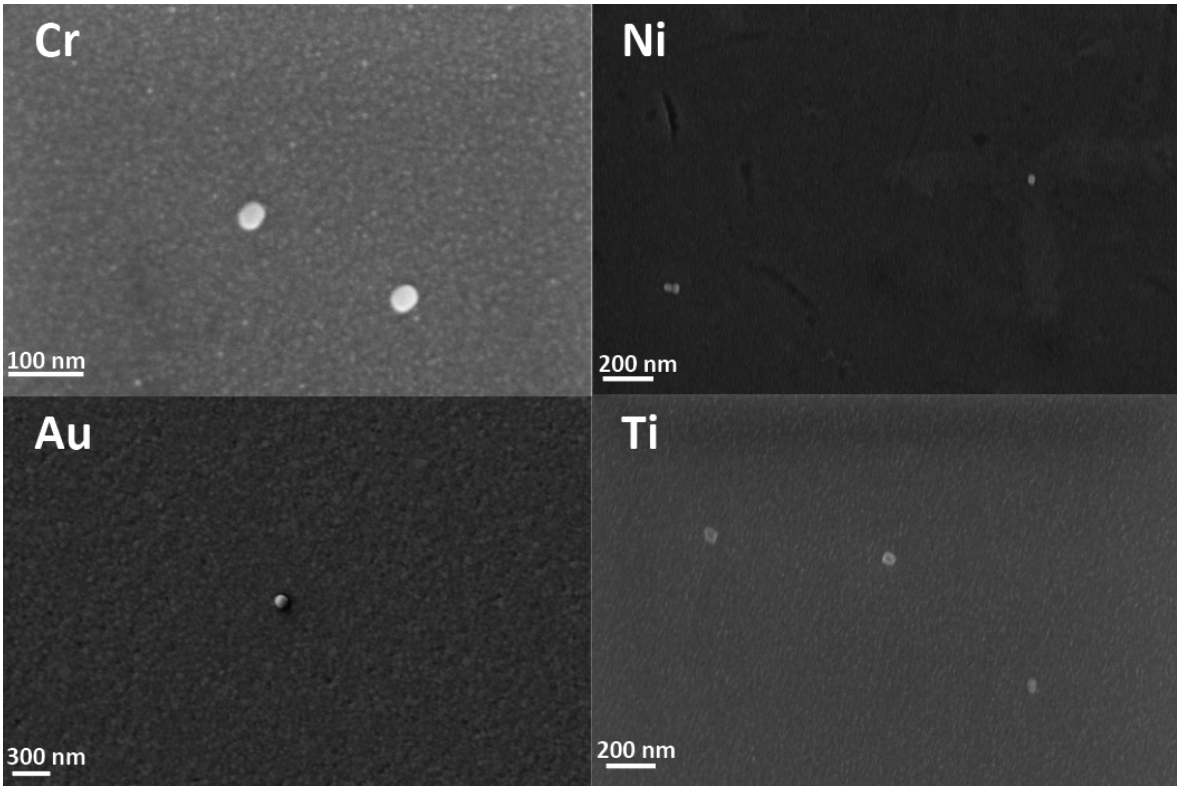

Fig. S5. Scanning electron microscope (SEM) images of UCNPs on the Cr-, Au-, and Ti-coated sapphire substrates and the Ni-coated glass substrate.

Note S1: Analytical calculations of the steady-state temperature rise

To assess the potential for laser heating resulting from continuous wave irradiation of our samples by the 976 nm excitation laser, we performed analytical calculations of the temperature rise under different experimental conditions. Axisymmetric heat conduction in layered systems incorporating radial effects can be analyzed using Hankel transforms. Detailed solutions are provided elsewhere in the literature[1,2], and here we briefly summarize the framework used to solve for the steady-state temperature rise, $\theta(r,z) = T(r,z) - T_\infty$, where r and z represent the radial and axial coordinates, respectively, and T_∞ represents the far-field sample temperature.

Considering a sample surface surrounded by an insulating medium such as air, as is the case in our experiments, the temperature rise and heat flux at the top of a layer i are related to the temperature rise and heat flux at the bottom of layer i by

$$\begin{bmatrix} \tilde{\theta}_{bottom,i}(q) \\ \tilde{Q}_{bottom,i}(q) \end{bmatrix} = \begin{bmatrix} \cosh(qd_i) & -\frac{1}{qk_i}\sinh(qd_i) \\ -qk_i\sinh(qd_i) & \cosh(qd_i) \end{bmatrix} \begin{bmatrix} \tilde{\theta}_{surface,i}(q) \\ \tilde{Q}_{surface,i}(q) \end{bmatrix} = \boldsymbol{M}_i \begin{bmatrix} \tilde{\theta}_{surface,i}(q) \\ \tilde{Q}_{surface,i}(q) \end{bmatrix}, \tag{S1}$$

where $\tilde{\theta}(q)$ and $\tilde{Q}(q)$ denote the Hankel transforms of the temperature rise and heat flux, respectively, q is the Hankel transform variable, and k_i and d_i represent the thermal conductivity and thickness, respectively, of layer i. For an n-layered system, the general solution can be expressed as

$$\begin{bmatrix} \tilde{\theta}_{bottom}(q) \\ \tilde{Q}_{bottom}(q) \end{bmatrix} = \boldsymbol{M}_n\boldsymbol{M}_{n-1}\ldots\boldsymbol{M}_1 \begin{bmatrix} \tilde{\theta}_{surface}(q) \\ \tilde{Q}_{surface}(q) \end{bmatrix} = \begin{bmatrix} \tilde{A} & \tilde{B} \\ \tilde{C} & \tilde{D} \end{bmatrix} \begin{bmatrix} \tilde{\theta}_{surface}(q) \\ \tilde{Q}_{surface}(q) \end{bmatrix}, \tag{S2}$$

with the matrix $\boldsymbol{M}_n$ corresponding to the bottom layer. If the nth layer is treated as semi-infinite, Eq. S2 leads to $\tilde{C}\tilde{\theta}_{surface}(q) + \tilde{D}\tilde{Q}_{surface}(q) = 0$. Subsequently, $\tilde{\theta}_{surface}(q)$ can be written as

$$\tilde{\theta}_{surface}(q) = -\frac{\tilde{D}}{\tilde{C}}\tilde{Q}_{surface}(q), \tag{S3}$$

and the Hankel transform of the heat flux at the top surface of the sample resulting from a Gaussian heat source is

$$\tilde{Q}_{surface}(q) = APexp\left(-\frac{q^2r_{laser}^2}{8}\right). \tag{S3}$$

Here, P is the laser power, which we measured at the sample plane, and A is the absorptance of the top layer, which we determined experimentally for the metal coatings used in our work,

as described below in Fig. S2 and Table S1. This analysis assumes that the incident laser light is absorbed at the sample surface, which is a reasonable approximation for the metal-coated samples used in this work. r_{laser} is the $1/e^2$ laser radius, which we experimentally determined to be approximately 623 nm by scanning a single 80 nm Au nanoparticle and recording the backscattered light to visualize the intensity profile of the Gaussian laser beam. Finally, the surface temperature rise can be expressed as

$$\theta_{surface}(r) = \frac{AP}{2\pi}\int_0^{\infty} -\left(\frac{\tilde{D}}{\tilde{c}}\right) exp\left(\frac{-q^2 r_{laser}^2}{8}\right) J_0(qr) q dq. \quad \text{(S4)}$$

This integral can be evaluated numerically, and the upper bound can in practice be reduced without loss of accuracy. Here, a bound of $10/r_{laser}$ was used, which was sufficient for all calculations performed. The peak temperature rise, which is the quantity of interest in this work, is the temperature rise at the center of the irradiated region, $\theta_{surface}(r = 0)$.

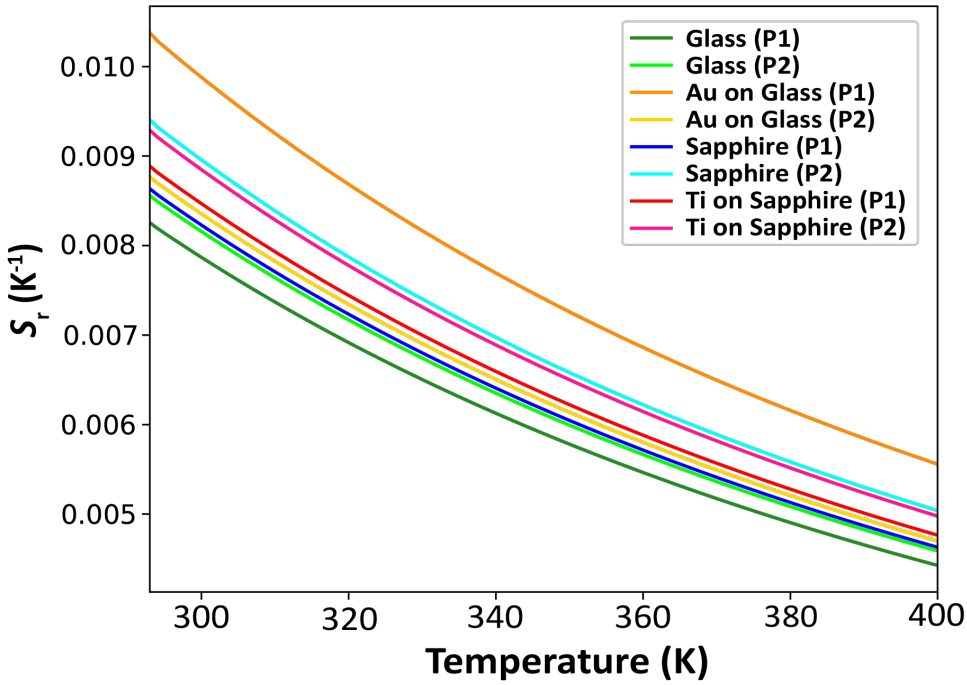

Fig. S6. A plot of the relative sensitivity S_r (defined as $S_r = \frac{1}{r}\frac{dr}{dT}$) vs. temperature for two individual UCNPs on each of four different substrates (uncoated borosilicate glass, Au-coated borosilicate glass, uncoated sapphire, and Ti-coated sapphire). The relative sensitivity values are calculated based on the corresponding fits to main text Eq. 1 for each particle, which are shown in main text Fig. 3b. The sensitivities are comparable to previously reported values in the literature for individual $NaYF_4$:Yb^{3+},Er^{3+} UCNPs[3] and UCNP ensembles[4].

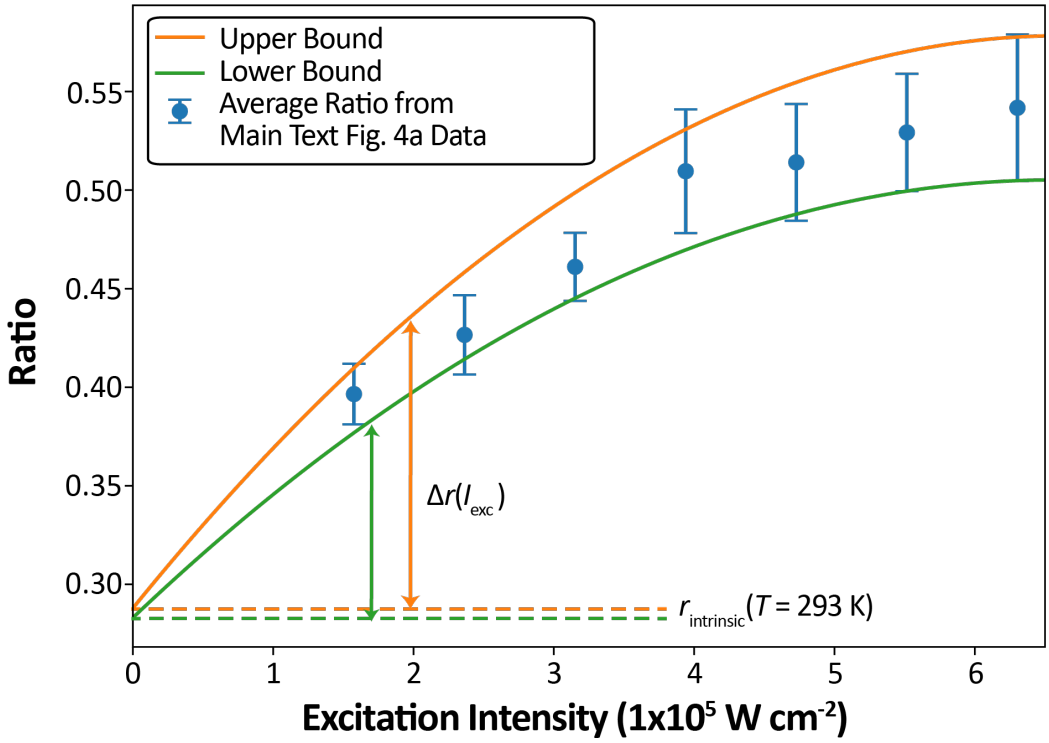

Fig. S7. A plot of the average luminescence intensity ratio (r) vs. excitation intensity (I_{exc}). The blue data points and error bars represent the average and standard deviation of the r values measured from single UCNPs on uncoated borosilicate glass and sapphire and Au- and Ag-coated borosilicate glass and sapphire for each I_{exc} value from the main text Fig. 4a. The orange line is a quadratic fit to the upper bounds of the error bars and defines the upper boundary of the blue shaded region in main text Fig. 4b. The green line is a quadratic fit to the lower bounds of the error bars and defines the lower boundary of the blue shaded region in main text Fig. 4b. The horizontal dashed lines indicate where the upper and lower bound fits intercept the y axis at 0.2878 and 0.2830, respectively, corresponding to $r_{intrinsic}(T = 293\ K)$. The two vertical arrows represent the two $\Delta r(I_{exc})$ values calculated from the fits to the upper and lower bounds of the error bars, respectively.

Note S2: Quantifying the $r(I_{exc})$ increase originating from the apparent self-heating contribution

Fig. S7 illustrates the process of determining the blue shaded band representing the apparent self-heating effect[5] in main text Fig. 4b. For each laser excitation intensity (I_{exc}), the average luminescence intensity ratio (r) for UCNPs on uncoated borosilicate glass and sapphire and Au- and Ag-coated borosilicate glass and sapphire was computed and is represented by the blue data points in Fig. S7. The error bars in Fig. S7 represent the standard deviation across all these samples, providing an upper and a lower bound on the $r(I_{exc})$ increase resulting from the apparent self-heating effect. The upper bounds of these error bars were fit using a quadratic function, $r(I_{exc}, T = 293\ K) = A \times {I_{exc}}^2 + B \times I_{exc} + r_{intrinsic}(T = 293\ K)$, and the resulting fit is represented as the orange line in Fig. S7, which corresponds to the upper boundary of the blue shaded band in main text Fig. 4b. Similarly, the lower bounds of these error bars were also fit using the same quadratic function. The resulting fit is represented as the

green line in Fig. S7 and corresponds to the lower boundary of the blue shaded band in main text Fig. 4b. These bounds capture the variation in the non-thermal apparent self-heating effect across UCNPs on different substrates. $r_{intrinsic}(T = 293\ K)$ is the r value corresponding to I_{exc} = 0 at room temperature that is extrapolated from the fitted curves. $\Delta r(I_{exc}) = A \times {I_{exc}}^2 + B \times I_{exc}$ represents the non-thermal apparent self-heating effect contribution to $r(I_{exc}, T)$. Two values of $\Delta r(I_{exc})$ are calculated from the upper and lower fits to the $r(I_{exc}, T = 293\ K)$ data, as shown in Fig. S7, to account for uncertainty in the apparent self-heating contribution when measured r values shown in main text Fig. 4b are converted to temperature rises, as detailed later in Note S3.

	A (x 10^{-13} cm^4 W^{-2})	B (x 10^{-7} cm^2 W^{-1})	$r_{intrinsic}(T = 293\ K)$
Upper Fit	-6.639	8.783	0.2878
Lower Fit	-5.157	6.7698	0.2830

Table S2. Fitted A, B, and $r_{intrinsic}(T = 293\ K)$ values corresponding to the upper and lower bounds of the apparent self-heating effect data shown in Fig. S7.

Note S3: Conversion from measured ratio values to temperature rises

The temperature rise data shown in main text Fig. 4c and the associated error bars were calculated as follows: first, we calculated $r_{intrinsic}(T)$, where the temperature T is undetermined, using $r_{intrinsic}(T) = r(I_{exc}, T) - \Delta r(I_{exc})$, where $r(I_{exc}, T)$ is the averaged value of two measurements at each I_{exc} on either Ni-, Cr- or Ti-coated borosilicate glass substrates shown in main text Fig. 4b. Conceptually similar to $r_{intrinsic}(T = 293\ K)$ discussed above, these calculated $r_{intrinsic}(T)$ values also represent r values free from non-thermal apparent self-heating contributions, but associated with an undetermined temperature T instead of room temperature. Meanwhile, we account for the uncertainty associated with the two values of $\Delta r(I_{exc})$, calculated from upper and lower fits shown in Fig. S7 and described in detail in Note S2. Therefore, two values of $r_{intrinsic}(T)$ were obtained for each data point in main text Fig. 4b.

Second, we extracted temperatures from these $r_{intrinsic}(T)$ values, which were obtained from uncalibrated single UCNPs, using the following batch calibration procedure: we began by fitting the measured $r(I_{exc}, T)$ values in main text Fig. 3b to main text Eq. 1 to calibrate eight single UCNPs on different substrates. The coefficients A and ΔE from main text Eq. 1 were calculated for each fit and are shown below in Table S3. Then, we calculated eight $r_{intrinsic}(T)$ functions by shifting the eight fitted $r(I_{exc}, T)$ curves down by the averaged value of two $\Delta r(I_{exc} = 1.58 \times 10^5\ W\ cm^{-2})$, where this I_{exc} corresponds to the value used for the temperature calibrations. These two $\Delta r(I_{exc} = 1.58 \times 10^5\ W\ cm^{-2})$ values were again calculated using the upper and lower fits reported in Fig. S7 and represent the non-thermal artifact introduced by the I_{exc} used for temperature calibration. These eight $r_{intrinsic}(T)$ functions, conceptually representing temperature calibrations performed with $I_{exc} = 0\ W\ cm^{-2}$, were applied to extract temperatures from the $r_{intrinsic}(T)$ values calculated from the measured $r(I_{exc}, T)$ data points shown in main text Fig. 4b. Sixteen temperature values were obtained by inputting two values of $r_{intrinsic}(T)$ into the eight different $r_{intrinsic}(T)$

functions. After subtracting the room temperature value (293 K), we plot the mean of these sixteen calculated temperature rises and represent the standard deviation as the error bars in main text Fig. 4c. Therefore, these error bars represent the uncertainty from the temperature batch calibration procedure, the variation of the non-thermal apparent self-heating effect for different single UCNPs on different substrates, and trial-to-trial variation. For the measurements shown in main text Fig. 4c, the temperature uncertainties for measurements on each metal coating range from ± 6 K to ± 12 K for Ni, ± 7 K to ± 13 K for Cr, and ± 11 K to ± 18 K for Ti. The temperature uncertainty increases with I_{exc} for each metal coating due to the greater uncertainty in the apparent self-heating contribution at higher I_{exc}, which can be observed in main text Fig. 4a and Fig. S7. Additionally, the uncertainties increase with the measured absolute temperature due to the increasing deviation among the fitted calibration curves shown in main text Fig. 3b at higher temperatures. As a result, at a fixed I_{exc}, the temperature uncertainty is highest for measurements on Ti and lowest for measurements on Ni.

	$\boldsymbol{A}$	$\boldsymbol{\Delta E}$
Glass (P1)	5.268	63.3
Glass (P2)	8.837	76.6
Au on Glass (P1)	5.863	64.8
Au on Glass (P2)	5.343	61.0
Sapphire (P1)	5.800	63.8
Sapphire (P2)	6.879	69.5
Ti on Sapphire (P2)	6.681	68.6
Ti on Sapphire (P1)	5.949	65.7

Table S3. Fitted A and ΔE values corresponding to main text Eq. 1 for eight single UCNPs on different substrates.

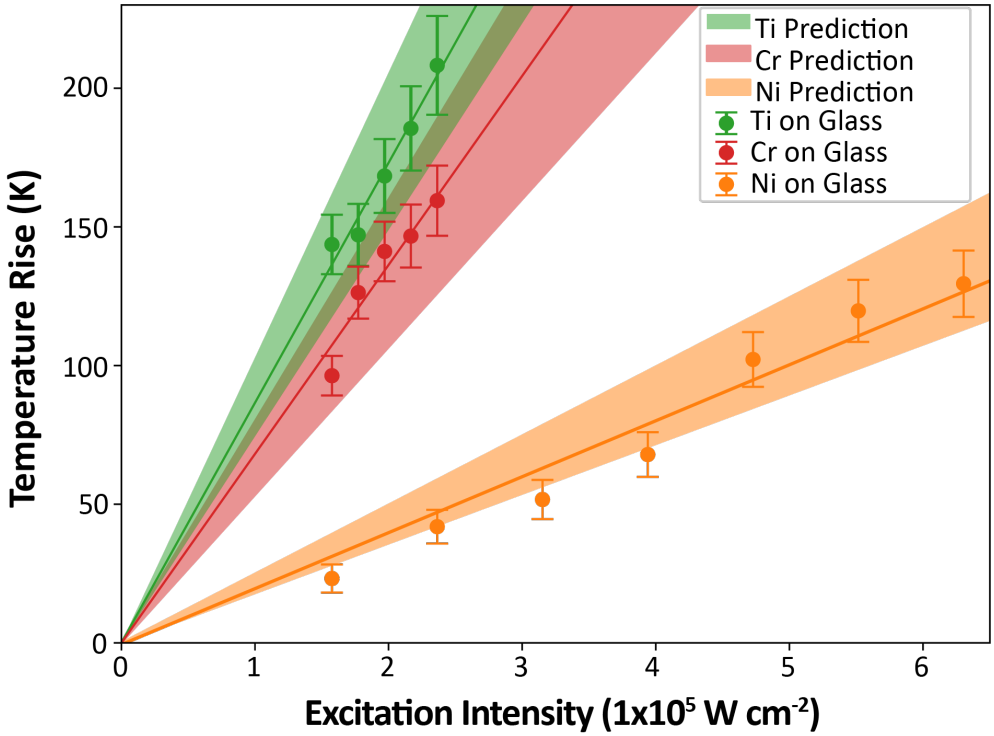

Fig. S8. Temperature rise measured by single UCNPs on Ni-, Cr-, and Ti-coated borosilicate glass (same data shown in main text Fig. 4c), along with corresponding analytical model predictions. For each metal coating, the shaded bands represent a range of possible thin-film thermal conductivity values, as shown in Table S4. The absorptance and thickness of the metal coating and the thermal conductivity of the substrate are fixed, and the coating thickness values are also shown in Table S4.

Metal coating	Thickness (nm)	Range of thermal conductivity (W m^{-1} K^{-1})
Ti	40	[4, 11]
Cr	40	[9, 23]
Ni	60	[57, 90]

Substrate	Thermal conductivity (W m^{-1} K^{-1})
Sapphire	40
Glass	1

Table S4: Thermal conductivity and coating thickness values used in the analytical heat transfer model to calculate the shaded bands shown in Fig. S8.

Note S4: Estimating the range of metal coating thermal conductivity values compatible with the experimental temperature rise data

To optimally match the experimental results with realistic parameters, we applied the analytical heat transfer model described in Note S1 to calculate the peak temperature rise of the metal surface due to laser heating. We use the absorptance values shown in Table S1. We input the metal coating thicknesses (which can deviate by up to ±20% from the nominal value of 50 nm) and the thermal conductivities of the substrates and metal coatings shown in Table S4 into the analytical model. For Ni-, Cr-, and Ti-coated borosilicate glass, where the measured ratio

values fall well above the blue shaded band shown in main text Fig. 4b, we vary the thermal conductivity of the metal coating considering reported bulk[6] and thin-film thermal conductivity values[7-9], the latter of which are typically reduced below the corresponding bulk values due to fabrication defects and increased boundary scattering. The resulting model predictions combined with the data points from the main text Fig. 4c are shown in Fig. S8.

Supplementary References:

1. J. L. Braun, C. J. Szwejkowski, A. Giri and P. E. Hopkins, *Journal of Heat Transfer*, 2018, **140**, 052801.
2. A. D. Pickel and C. Dames, *Journal of Applied Physics*, 2020, **128**, 045103.
3. J. D. Kilbane, E. M. Chan, C. Monachon, N. J. Borys, E. S. Levy, A. D. Pickel, J. J. Urban, P. J. Schuck and C. Dames, *Nanoscale*, 2016, **8**, 11611-11616.
4. F. Vetrone, R. Naccache, A. Zamarrón, A. Juarranz de la Fuente, F. Sanz-Rodríguez, L. Martinez Maestro, E. Martín Rodriguez, D. Jaque, J. García Solé and J. A. Capobianco, *ACS Nano*, 2010, **4**, 3254-3258.
5. A. D. Pickel, A. Teitelboim, E. M. Chan, N. J. Borys, P. J. Schuck and C. Dames, *Nature Communications*, 2018, **9**, 4907.
6. Y. S. Touloukian, R. W. Powell, C. Y. Ho and P. G. Klemens, *Thermophysical Properties of Matter - The TPRC Data Series. Volume 1. Thermal Conductivity - Metallic Elements and Alloys*, 1971.
7. Y. Zeng, L. a. Li, S. Wang, F. Sun, Z. Wang, X. Tu and C. Li, *International Journal of Heat and Mass Transfer*, 2024, **227**, 125542.
8. K. L. Zhang, S. K. Chou and S. S. Ang, *International Journal of Thermal Sciences*, 2007, **46**, 580-588.
9. L.-D. Zhu, F.-Y. Sun, J. Zhu, D.-W. Tang, Y.-H. Li and C.-H. Guo, *Chinese Physics Letters*, 2012, **29**, 066301.